

# Interfacial Curvature in Confined Coculture Directs Stromal Cell Activity with Spatial Corraling of Pancreatic Cancer Cells

Stephanie Nemeč, Joey Lam, Jingxiao Zhong, Celine Heu, Paul Timpson, Qing Li, Janet Youkhana, George Sharbeen, Phoebe A. Phillips, and Kristopher A. Kilian\*

Interfacial cues in the tumor microenvironment direct the activity and assembly of multiple cell types. Pancreatic cancer, along with breast and prostate cancers, is enriched with cancer-associated fibroblasts (CAFs) that activate to coordinate the deposition of the extracellular matrix, which can comprise over 90% of the tumor mass. While it is clear that matrix underlies the severity of the disease, the relationship between stromal-tumor cell assembly and cell-matrix dynamics remains elusive. Micropatterned hydrogels deconstruct the interplay between matrix stiffness and geometric confinement, guiding heterotypic cell populations and matrix assembly in pancreatic cancer. Interfacial cues at the perimeter of microislands guide CAF migration and direct cancer cell assembly. Computational modeling shows curvature-stress dependent cellular localization for cancer and CAFs in coculture. Regions of convex curvature enhance edge stress that activates a myofibroblast phenotype in the CAFs with migration and increased collagen I deposition, ultimately leading to a central “corralling” of cancer cells. Inhibiting mechanotransduction pathways decreases CAF activation and the associated corralling phenotype. Together, this work reveals how interfacial biophysical cues underpin aspects of stromal desmoplasia, a hallmark of disease severity and chemoresistance in the pancreatic, breast, and prostate cancers, thereby providing a tool to expand stroma-targeting therapeutic strategies.

## 1. Introduction

The vast stroma/desmoplasia produced by cancer-associated fibroblasts (CAFs) is clinically characteristic of pancreatic ductal adenocarcinoma (PDAC) and contributes to poor therapeutic response.<sup>[1–3]</sup> PDAC arises from precursor lesions called pancreatic intraepithelial neoplasia (PanINs), that develop from the exocrine compartment of the pancreas (lobular acinar cells, centro-acinar, and duct cells).<sup>[4]</sup> Pancreatic CAFs engage in bidirectional interactions with pancreatic cancer cells and once activated become myofibroblast-like, generating and coordinating stroma.<sup>[5–7]</sup> Throughout PDAC progression, CAFs are dynamic, surrounding and infiltrating the primary tumor, as well as reorganizing collagen and fibronectin fibrils.<sup>[8]</sup>


Cells respond to biophysical cues in their microenvironment through mechanotransduction pathways.<sup>[9,10]</sup> For example, cancer progression and specific states associated with invasive phenotypes have been linked to matrix stiffness,<sup>[11]</sup> softness,<sup>[12]</sup> stretch,<sup>[13]</sup> nano- and micro-

topography.<sup>[14,15]</sup> For PDAC in particular, the stiff extracellular matrix created by the fibrotic cells disrupts the homeostasis of

S. Nemeč, Prof. K. A. Kilian  
School of Materials Science and Engineering  
UNSW Sydney  
Sydney, NSW 2052, Australia  
E-mail: k.kilian@unsw.edu.au

J. Lam, Prof. K. A. Kilian  
School of Chemistry Australian Centre for Nanomedicine  
UNSW Sydney  
Sydney, NSW 2052, Australia

J. Zhong, Prof. Q. Li  
School of Aerospace, Mechanical and Mechatronic Engineering  
The University of Sydney  
Sydney, NSW 2006, Australia

 The ORCID identification number(s) for the author(s) of this article can be found under <https://doi.org/10.1002/adbi.202000525>.

Dr. C. Heu  
Biomedical Imaging Facility  
Mark Wainwright Analytical Center  
UNSW Sydney  
Sydney, NSW 2052, Australia

Prof. P. Timpson  
The Kinghorn Cancer Centre  
Garvan Institute of Medical Research  
Sydney 2052, Australia

J. Youkhana, Dr. G. Sharbeen, Prof. P. A. Phillips  
Pancreatic Cancer Translational Research Group  
Lowy Cancer Research Centre  
School of Medical Sciences  
UNSW Sydney  
Sydney, NSW 2052, Australia

DOI: 10.1002/adbi.202000525

the native microenvironment, enhancing their mechanosensitivity. Forces on the cell surface are perceived by complexes including integrins that can cluster, triggering focal adhesion kinase driving local mechanochemical signaling that culminates in a disrupted, nonuniform organization comprising heterogeneous PDAC.<sup>[16]</sup> These biophysical and biochemical cues are amplified by further activating CAFs to secrete a host of cytokines promoting cancer-associated fibroblast crosstalk prompting tumorigenesis and therapeutic resistance.<sup>[17]</sup>

In vivo, fibroblasts comprise 4% of healthy pancreas and proliferate and activate into CAFs comprising 50–80% of PDAC tumor volume, depending on the patient.<sup>[18,19]</sup> Most model systems target a similar ratio of cancer to CAFs from 2:1 majority cancer to 1:2 majority CAFs and employ a variety of media sources from standard media to organoid-enriched media laden with differentiation inhibitors. Coculture models incorporating PDAC and CAFs typically rely on anchorage independent culture. These 3D cancer spheroids and cocultured organoids can range from 40  $\mu\text{m}$  to over 1 mm in diameter.<sup>[20,21]</sup> Microfluidics have been employed to promote coculture interaction and investigate migration with drug-laden media.<sup>[22,23]</sup> Various embedding techniques such as hanging drop and postenabled polymerization and material suspension in Matrigel, collagen I, and methylcellulose enable embedding of primary derived or immortalized cell lines of cancer and patient matched CAFs.<sup>[21,24,25]</sup> A commonality to all in vitro pancreatic cancer models is the tendency for similar cells to assemble—PDAC cluster segregation coupled with interpenetrating CAF cell structures—thereby providing spatial organization that is reminiscent of in vivo tissue.

The last several decades have seen the development of engineered extracellular matrices, where cues in the tumor microenvironment can be precisely controlled to study cancer progression. Engineered substrates have been used to explore the epithelial-to-mesenchymal (EMT) transition in PDAC, defining heterotypic CAF activation and stroma production, which enhanced a chemoresistant state that can be used to develop patient-specific treatment.<sup>[26,27]</sup> Matrix micropatterning techniques have provided means to study the role of geometry and cell–cell connectivity in directing functional outcomes in cancer at the single cell<sup>[28]</sup> to multicellular levels.<sup>[29]</sup> The majority of cell micropatterning studies are based on a single cell type, largely because heterotypic cocultures lead to heterogeneous populations that obscure useful or biological relevant read-outs. Fukuda et al. used a sequential patterning approach to pattern hepatocytes with fibronectin followed by fibroblasts onto collagen, while Mukundan et al. similarly leveraged collagen with nonadherent Pluronic F-127 to pattern primary PDAC cells then washed and surrounded with pancreatic CAFs.<sup>[30,31]</sup> While there are numerous examples of PDAC and stromal cell cocultures for fundamental studies, mouse models, and drug development efforts, the role of microenvironment parameters such as cancer/CAF/matrix interaction and remodeling in directing stromal cell activity and accompanying PDAC organization is not well understood.<sup>[32]</sup>

The assembly of cancer cells and surrounding stroma in vivo is orchestrated through a multivariate assortment of extracellular cues. Here we use a hydrogel micropatterning approach based on soft lithography to explore heterotypic signaling between CAFs and PDAC cells as a function of matrix stiff-

ness and interfacial geometry. Using computational modeling and tracking cellular localization, we identify mechanical stress patterns at the perimeter of microislands that drive a myofibroblast phenotype in the CAF population that corresponds to a central “corralling” of the cancer cells. Understanding the interplay between biophysical aspects of the microenvironment and cellular organization will assist efforts for developing interventions that target matrix in pancreatic cancer.

## 2. Results

### 2.1. Geometric Confinement Directs Pancreatic Cancer and CAF Assembly

The pancreatic cancer microenvironment contains dense stroma/desmoplasia generated by cancer-associated fibroblasts.<sup>[27,33]</sup> Coculture models of PDAC cells and CAFs can capture cellular crosstalk between the associated cells;<sup>[20,21,34]</sup> however, the influence of physical and mechanical cues on the coculture has yet to be investigated. To study how PDAC–stroma interactions may guide assembly in culture, we employed a microcontact printing approach using polyacrylamide hydrogels of variable stiffness that are chemically modified to present distal hydrazine functionality for subsequent stamping of oxidized matrix protein to form a stable hydrazone linkage.<sup>[15,35,36]</sup> To ensure we have consistent matrix deposition and mechanical properties across the patterned shapes, we deposited fluorescently labeled fibrinogen and fibronectin and performed simultaneous fluorescence imaging and atomic force microscopy (AFM) across the hydrogels. Figure S1 of the Supporting Information shows our protein conjugation leads to uniform patterning with no significant difference in gel stiffness across shapes on account of microcontact printing. We used PDAC cells and CAFs derived from the transgenic mouse KPC tumors,<sup>[37]</sup> labeled with variable color CellTracker: 492/517 (green) for PDAC cells and 577/602 (red) for CAFs, combined in equal ratio (1:1) and dispersed the cells on fibronectin-micropatterned polyacrylamide gels (**Figure 1A**). After 2 days on the patterns, shape-induced self-organization—localization of cancer cells toward the center of the pattern—occurred on circles (50 000  $\mu\text{m}^2$ ) compared to nonpatterned gels (blank polydimethylsiloxane (PDMS) stamped) (**Figure 1B**). In the patterned culture, we observed concentric organization of PDAC cells at the interior, surrounded by stroma at the perimeter of the micropatterns, with 96% of patterns displaying this spatial organization. This contrasts with the nonpatterned condition, and previous models of PDAC cells:CAF cocultures,<sup>[21,34,38,39]</sup> where the cancer cells and CAFs display random organization across the surface. Observing this localization, we probed various regions—a central cancer-rich and peripheral CAF-rich area—of the pattern using AFM that showed an average stiffness of 15.6 kPa on the hydrogel which dropped to 520 Pa for the peripheral CAF population and increased to 970 Pa for the central PDAC (**Figure S2**, Supporting Information). The AFM derived stiffness across the circular microislands enables creation of a shape-induced stress profile using a finite element (FE) model visualizing the von-Mises stress (Pascals, Pa) (**Figure 1C**). These results demonstrate how geometric

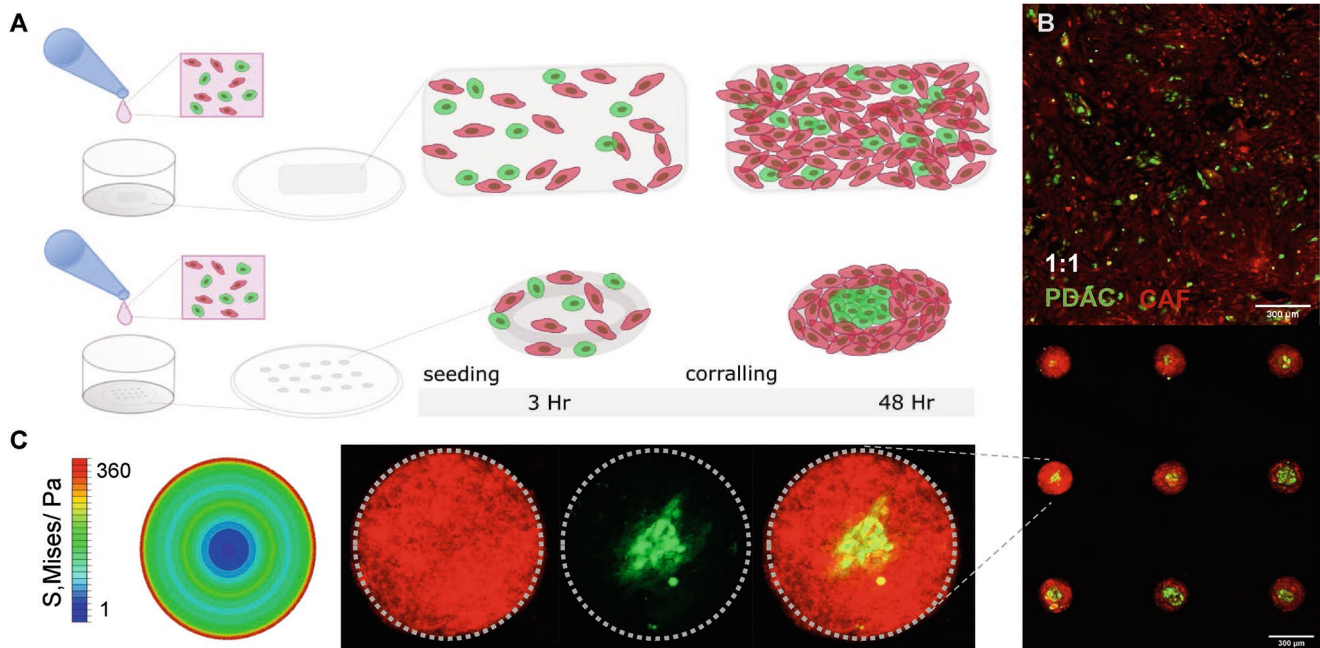


**Figure 1.** Schematic of equal ratio pancreatic cancer and CAF cell addition to fibronectin micropatterns with coculture localization. A) Primary murine KPC pancreatic cancer cells and cancer-associated fibroblasts (CAFs) cells lifted from 2D culture plates. Cancer cells labeled with CellTracker green (492/517) and CAFs labeled with CellTracker red (577/602) then counted, mixed in equal number and added to fibronectin micropatterns (gray shade) stamped on nonadherent polyacrylamide gels. B) Immunofluorescence image of cocultured cellular response to nonpattern (top) and circle (bottom, 250  $\mu\text{m}$  diameter) patterns of representative widefield microscopy area. Cancer cells migrate toward the central region and CAFs to the outer regions when confined to circle patterns. Zoom in on single circle pattern with red CAF and green cancer cell with merge. C) ABAQUS finite element model of von-Mises stress (Pascals, Pa) of coculture (cancer: CAF) cells on circle substrate.

confinement and interfacial stress may coordinate interactions between PDAC cells and support cells under confinement in culture.

## 2.2. Hydrogel Stiffness Influences Cancer Corralling by CAFs Through Altered Migration

Having observed cell segregation in microconfinement, we sought to explore if the underlying stiffness of the substrates would influence the spatial assembly in our micropatterned coculture. We selected a range of polyacrylamide gel stiffness (1, 10, and 100 kPa) that encompasses all soft tissues. Healthy pancreas has a stiffness around 1 kPa and pancreatic tissue progressively stiffens to  $\approx 4\text{--}8$  kPa PDAC.<sup>[40]</sup> On stiff culture substrates like polystyrene tissue culture plastic, CAFs stretch and activate to a myofibroblastic phenotype.<sup>[41,42]</sup> We seeded our 1:1 ratio coculture of cancer and CAFs labeled with CellTracker (40 000 cells  $\text{mL}^{-1}$ ) on micropatterned circular islands across stiffness-tuned polyacrylamide gels. After settling for 3 h, the cocultures were imaged every hour over 2 days to visualize cell-cell interactions and migratory behavior.

We found the green-labeled cancer cells migrated toward the center across substrates of all tested stiffness (Movies S1–S3, Supporting Information), while red-labeled CAFs moved toward the periphery of the circle patterns (Figure 2A). Time-based cell tracks indicated cancer cells began on the outside of the pattern

and moved centrally over 48 h (Figure 2B). As predicted by previous work,<sup>[43,44]</sup> cancer cells move faster on stiffer materials with an average speed of  $0.19 \mu\text{m min}^{-1}$  on 100 kPa compared to  $0.10 \mu\text{m min}^{-1}$  on 1 kPa. However, the averaged direction was more varied at higher stiffnesses compared to lower based on a quantitation of movement directionality (Figure 2C). Although the cells moved fastest on the stiffest 100 kPa polyacrylamide substrate, the clustering of cancer cells is tightest on 10 kPa hydrogels. Overall, the quality of the clustering is best in the 10 kPa, followed by the 100 kPa, and lastly the 1 kPa where cells moved the slowest and comparatively localized toward the edge after 48 h of culture.

## 2.3. Confinement-Induced Interfacial Stress Influences Coculture Assembly and Localization

In addition to matrix stiffness, tissue assembly is coordinated by interfaces that impose topological constraints.<sup>[45]</sup> To investigate the role of geometry in coordinating the cancer cell corralling observed in our coculture, we varied perimeter curvature using micropatterned islands of the same area approximating a circle, flower, and star shape, where we postulate that varying degrees of positive and negative curvature at the boundary will influence organization. Identical culture conditions were controlled with 40 000 cells  $\text{mL}^{-1}$  seeding density for 48 h. We found no statistical difference in the total nuclei count nor the



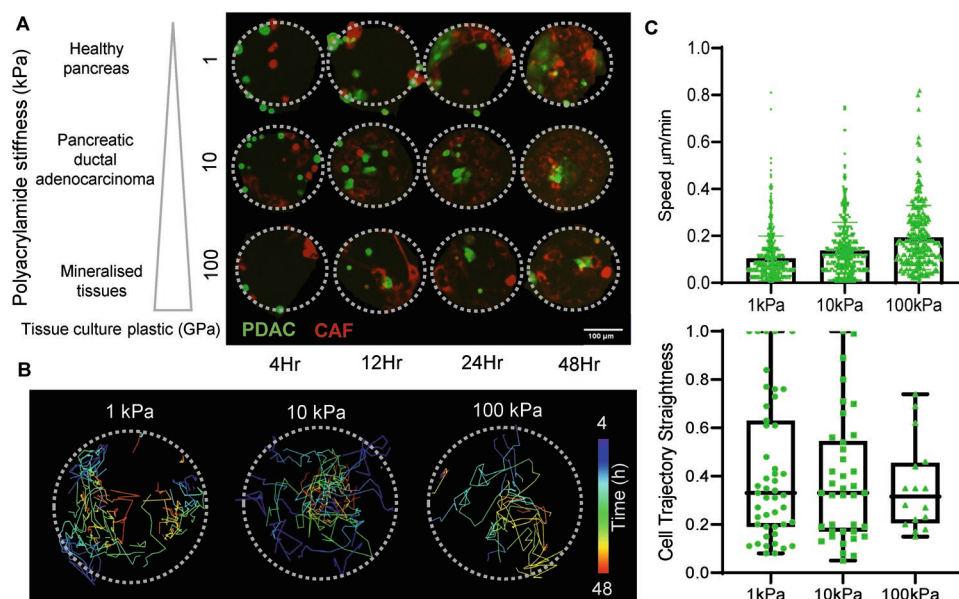


**Figure 2.** Polyacrylamide gel stiffness influence CAF corralling of cancer cells. A) Time series 4, 12, 24, 48 h time points of 1, 10, 100 kPa stiffness coculture migration on circle patterns. Cancer cells labeled with CellTracker green, CAFs CellTracker red. B) Cell trajectory of coculture 4 to 48 h after seeding on circle micropatterns of varying stiffness. Colors mapping of cool-tones identifying early locations and progressing toward warm-colors of later time points. C) Cancer cell speed throughout the duration of the culture was averaged  $0.10$ ,  $0.14$ ,  $0.19 \mu\text{m min}^{-1}$  on 1, 10, and 100 kPa polyacrylamide gels, respectively, with mean and standard deviation plotted. Track straightness of cancer cells was calculated with the track displacement divided by track displacement length and average  $0.42$ ,  $0.38$ ,  $0.36$  (unitless) for respective 1, 10, 100 kPa polyacrylamide gels. All points were plotted with 1–99% box plot and min and max errors bars.

cancer and CAF count of cocultures on circle, flower, and star, with cell counts  $116 \pm 50$ ,  $98 \pm 33$ , and  $124 \pm 39$ , respectively (Figure 3A). While the cocultures attached and proliferated similarly across patterns, each cell type showed a variable pro-

pensity for regional migration according to perimeter curvature. Cancer cell localization to the center is most prominent in circle micropatterns compared to flower and star (Figure 3B). The localization intensity profile for circular cocultures shows

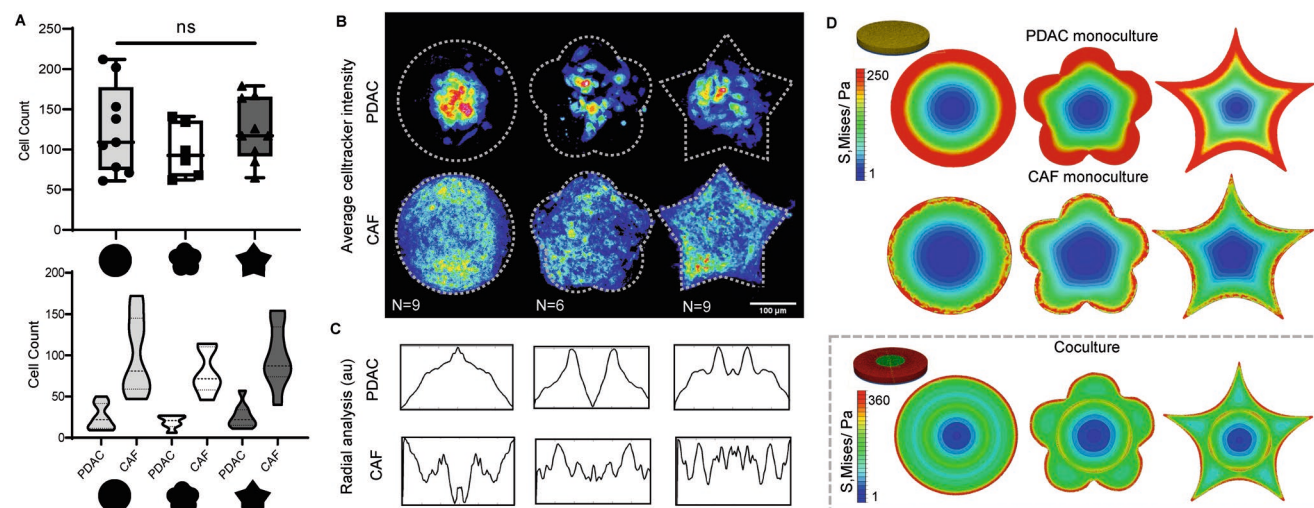


**Figure 3.** Circle, flower, and star micropatterns influence coculture self-assembly and FEM modeling of mono- and coculture. A) Box plot of total cell count per pattern; average  $\pm$  standard deviation circle  $116 \pm 50$ , flower  $98 \pm 33$ , star  $124 \pm 39$  (top). No significant (ns) difference in total cell number across patterns. Violin plot of cancer cells and CAFs; average  $\pm$  standard deviation of PDAC, CAF respectively for circle:  $25 \pm 16$ ,  $100 \pm 47$ , flower:  $19 \pm 8$ ,  $79 \pm 27$ , star:  $26 \pm 14$ ,  $99 \pm 37$  (bottom). B) Heatmaps of average z-projections of pancreatic cancer (top) and CAF (bottom) of circle ( $n = 9$ ), flower ( $n = 6$ ), star ( $n = 9$ ): patterns. C) Radial analysis with ImageJ radial reslice or average z-projections of cancer (top), CAF (bottom) cell heatmaps of gray value arbitrary units (a.u.) versus pixel distance from center on circle (left), flower (middle), and star (right) patterns. D) Meshed FEM models in ABAQUS with loading and boundary conditions of monoculture and coculture with CAFs at the periphery (red) and cancer cells in the center (green); FEM results of von-Mises stress contour on coculture cell sheets of CAFs alone in monoculture (top), cancer monoculture (middle), and coculture (bottom).

a single peak at the center, which contrasts with the multipeak profile for cocultures in flower and star patterns. Semiquantitative radial analysis of immunofluorescence heatmaps of fluorescence localization across multiple images indicate the highest intensity within the circular aggregates as central (125  $\mu\text{m}$  from the edge), compared to an averaged centralized peak intensity of 30  $\mu\text{m}$  off-center for the star aggregates and 44  $\mu\text{m}$  off-center for the flower aggregates. Consistent with these profiles, the CAFs show maximal localization at the perimeter of the circle with a trough in the center, which moves toward a periodically varying profile (Figure 3C).

To explore whether corraling was limited to the fibronectin protein coating, we also tested collagen I and laminin conjugation. Irrespective of protein composition, the centralization of cancer cells was consistent in these experiments (Figure S3, Supporting Information). In addition, we asked whether pattern size may play a role in the extent of corraling; larger interconnected patterns that do not inhibit cell migration led to a heterogeneous distribution of both cell types, thereby confirming out results where geometry directs spatial segregation (Figure S4, Supporting Information). Together this data reveals a picture where the stress fostered by interfaces will exert an influence on the radial organization of both CAF and cancer cells. We speculate that the balance between low stress regions and high stress regions provides mechanical cues that provide impetus for migration and localization to regions of elevated stress for mesenchymal cells (CAF) and to an energy minimum for cells with more epithelial character (cancer), which occurs irrespective of cancer, CAF ratio and attachment time (Figure S6, Supporting Information). However, we acknowledge that more work needs to be done to relate observed migration and localization to quantitative forces on the cell and the deformable substrate.

#### 2.4. Modeling Pancreatic Cancer, CAF, and Coculture Stress Induced by Micropatterning

One primary difference between these shapes is the stress a cell is expected to experience at the perimeter dictated by the curvature at the edge.<sup>[15,46,47]</sup> Computational modeling through finite element method of a contractile monolayer of cells—where a thermal gradient at the cell–hydrogel interface is imposed—demonstrate the highest region of stress at the perimeter with the lowest at the center of the pattern. As shown in previous work, regions of positive curvature (convex; circle and flower) impose higher stress on cells than regions of negative curvature (concave; star).<sup>[15,47]</sup> For a single cell type in culture, our finite element analysis demonstrates a gradual reduction of von-Mises stress from the border of the patterns toward the center, with stress concentrations varying across the concave and convex perimeter regions. It is also noted that models with cancerous cells experienced higher stress level than that of models with noncancerous, CAFs (Figure 3D).

Computational modeling of multiple cell types within a single patterned region has not been shown previously. To do this, we changed the Young's moduli of the 20  $\mu\text{m}$  contractile layer of cells according to experimentally determined stiffness via atomic force microscopy measurements (Figure S6,

Supporting Information) to represent noncancerous CAF and cancerous PDAC monolayers, 0.52 and 0.97 kPa, respectively, keeping the thermal conductivity and expansion coefficient constant across all models (Table S1, Supporting Information). For coculture, we defined a cancerous center with a noncancerous outer region and modeled how this would influence stress distribution in cocultures confined to circle, flower, and star shapes (Figure 3D). The cocultured models experienced the similar stress concentration patterns at the concave/convex borders of each micropattern. Among the three micropatterns, the circle pattern had less significant stress concentration at the CAF–cancer interface, compared to the star and flower patterns. This is because similar to the pattern-edge the anisotropic curvature with nodes enhances stress at the confined region compared to the isotropic circle pattern. While the volume averaged von-Mises stress exerted by cancerous cell layers varied across the patterns 107, 119, and 126 Pa for circle, flower, and star patterns and for the CAF cell layers 154, 177, and 162 Pa, respectively, the coculture patterned stress was 142, 154, and 149 Pa, respectively. It is demonstrated that, as cancer cells migrated toward the center of each pattern, the stress reduced from the border of each micropattern toward the center, with greatest radial uniformity in the circle followed by star then flower micropatterns (Figure 3D).

#### 2.5. Perimeter Curvature and Actomyosin Contractility Regulates CAF Activity and Spatial Organization in Coculture

This 2D hydrogel coculture model allows us to observe interactions between CAFs and cancer cells in response to pattern curvature. Next, we asked whether migration-localization behavior corresponds to characteristic phenotypes. A hallmark of CAF activation that underlies stroma/desmoplasia, is the myofibroblast-like phenotype.<sup>[48]</sup> To investigate whether CAFs in our micropatterned populations were undergoing this shift in response to interfacial stress, we immunostained patterned culture for a myofibroblast/CAF marker  $\alpha$ -smooth muscle actin ( $\alpha$ -SMA). We see increased  $\alpha$ -SMA expression at the periphery of our micropatterned aggregates compared to cells on nonpatterned hydrogels, and the occurrence and intensity of  $\alpha$ -SMA tracks with our localization and stress analysis (Figure 4A). When comparing across patterns we see that  $\alpha$ -SMA is most pronounced in cells in the flower geometry followed by cells in the circle, with cells in the star shape showing the most diffused, less-localized staining. A prominent role of the myofibroblast state is the synthesis and deposition of collagen I during stromal desmoplasia. Collagen I is an extracellular matrix protein produced by CAFs that can contribute to the dense stroma formed in PDAC. Immunostaining reveals significant colocalization of collagen I deposition and  $\alpha$ -SMA expression in the cocultures (Figure 4A).

To perturb the mechanical interaction yet allow attachment to the pattern, we investigated two actomyosin network inhibitors. Both blebbistatin, a myosin-II inhibitor, and further upstream Y27632, a Rho-associated protein kinase (ROCK) inhibitor, were added to the cell solution before seeding on patterns with Y27632 identified as an inactivator of CAFs.<sup>[49]</sup> Incorporation of these inhibitors decreased the expression of  $\alpha$ -SMA, leading to a more uniform staining across all patterned cells (Figure 4). In



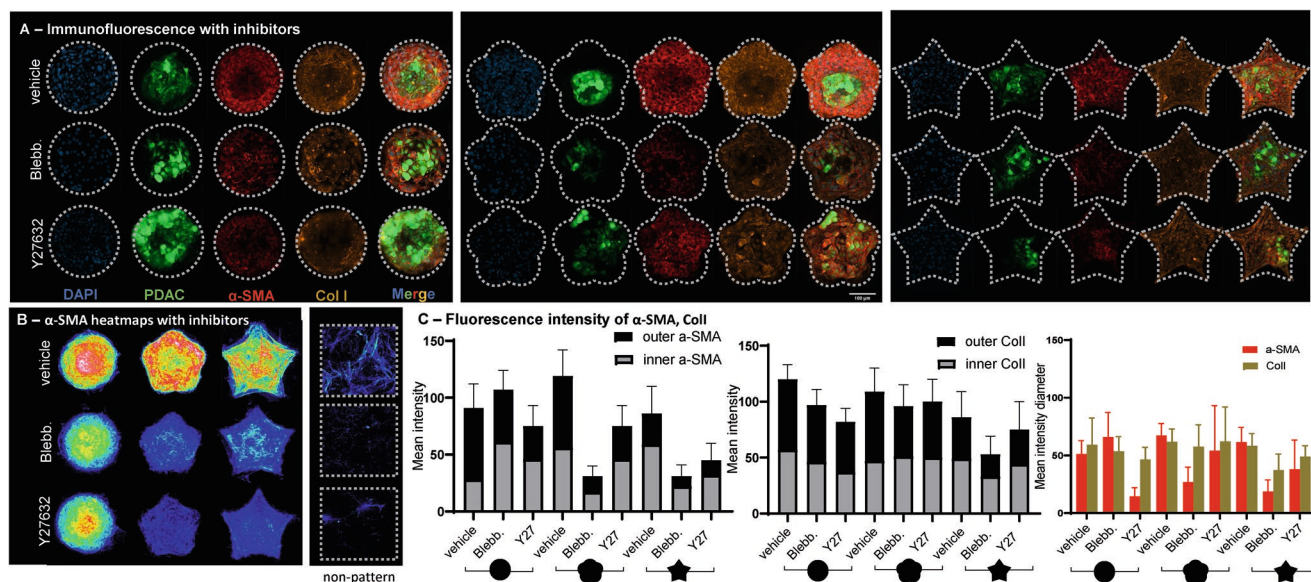


**Figure 4.** Mechanotransduction inhibitors decrease CAF activation on patterns. A) Immunofluorescence images of media control (vehicle) myosin-II inhibitor Blebbistatin (Blebb.) and ROCK inhibitor Y27632 (Y27) coculture pancreatic cancer and CAFs nuclear (DAPI), cancer cells labeled with Cell-Tracker green, CAF active, myofibroblast marker alpha-muscle actin ( $\alpha$ -SMA) 647 on circle, flower, and star patterns. Scale bras: 100  $\mu$ m. B) Heatmap projections of CAF activation, myofibroblast marker alpha-muscle actin ( $\alpha$ -SMA) 647 on circle, flower, and star patterns ( $n = 8$ ) and nonpattern ( $n = 3$ ). C) Quantification of  $\alpha$ -SMA, collagen I (Coll) mean fluorescence intensity of an inner circle (26%), flower (24%), and star (22%) region and outer calculated mean by dividing integrated density by area. Right: mean fluorescence intensity of  $\alpha$ -SMA and Coll across a diameter (223  $\mu$ m) of the respective patterns with standard deviation shown with error bars ( $n = 8$ ).

agreement with previous reports, Y27632 greatly decreased  $\alpha$ -SMA in CAFs across all patterns (Figure 4B). To further unravel the differences between inhibitors on CAFs, we observed collagen I expression in cocultures versus monoculture of circle, flower, star patterns. Heatmaps ( $n > 8$ ) indicate greater collagen intensity across all shapes and a marked retention in coculture compared to the CAF-only shapes with both blebbistatin and Y27632 inhibitors (Figure 5). This finding suggests that while disruption of actomyosin contractility will attenuate collagen deposition from stromal cells, heterotypic cocultures—particu-

larly in patterns with stress-inducing interfacial positive curvature—are able to maintain matrix synthesis and deposition.

### 3. Discussion

Pancreatic cancer tissue has a characteristic dense stroma and matrix which often corresponds with poor prognosis and outcome.<sup>[50]</sup> It is widely accepted that heterotypic interactions between PDAC cells and resident fibroblast subpopulations

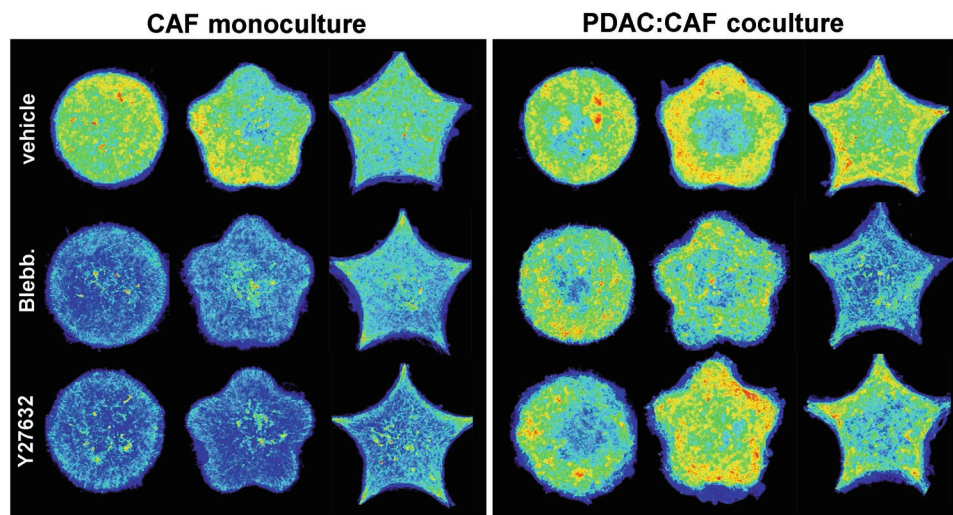


**Figure 5.** Shape-induced CAF and PDAC:CAF matrix deposition. Left: Heatmap projections collagen I (Coll) production of monoculture CAFs. Right: Cocultured pancreatic cancer and CAFs on circle, flower, and star patterns with inhibitors (Blebbistatin, Y27632) ( $n \geq 8$ ).

contributes to the regulation of matrix deposition and stromal desmoplasia.<sup>[51]</sup> Bolm et al. showed fibroblasts (NIH 3T3) promoted motility of several immortalized pancreatic cancer cell lines via paracrine signaling, and conversely pancreatic cancer elicited fibroblast activation.<sup>[52]</sup> Growth factors such as transforming growth factor, vascular endothelial growth factor, and platelet derived growth factor trigger CAF activation and desmoplastic reaction through enhanced proliferation by EMT transition.<sup>[53]</sup> By this extensive crosstalk between cancer and CAF in pancreatic cancer, not only can CAFs promote EMT, but they also migrate with pancreatic cancer cells and enable intravasation.<sup>[54,55]</sup>

Previously, we showed how geometry and mechanics can influence cell state across numerous human cancers.<sup>[15]</sup> In pancreatic cancer, others have shown micropatterned cancer cells surrounded by associated stromal cells display enhanced transport, metabolism, and invasive potential at the interface and drug-sensitive phenotypic heterogeneity.<sup>[56,57]</sup> While monocultured cancer spheroids are well studied, cocultured cancer and stromal cells have yet to be directed spatiotemporally in a reproducible model. Here we optimized our hydrogel microfabrication chemistry to confine mixtures of PDAC cells and CAFs in islands with variable perimeter geometry, to decouple multiple biophysical inputs in regulating cellular assembly in coculture.

In agreement with literature, CAF activity was further decreased by disrupting ROCK (Y27632) compared to Myosin II (Blebbistatin) in our micropatterned cocultures. Surprisingly, although the inhibitors decreased the CAF activity, the coculture organization was not significantly altered. One potential explanation is the PDAC–CAF interaction contributes to the coculture organization and thus when the inhibitors decrease cell contractility, there is continued segregation due to endogenous affinity between the different cell types. The persistent PDAC clustering, especially in the circle pattern, indicate a reduction in the persistence of micropatterned cues and cellular crosstalk between the CAF and cancer cells. This is likely due to multiple mechanotranscriptional pathways that continue to facilitate CAF activity through mechanisms beyond matrix engagement, e.g., paracrine and juxtacrine signaling.<sup>[58]</sup> For instance, in endothelial linings when vascular endothelial cadherin interactions are disrupted promoting vascular permeability, cytoplasmic binding partners enhance cell signaling to inhibit endocytosis and stabilize the endothelium.<sup>[59]</sup>

Self-organization is a property of cells that has taken center stage in the development of tissue-like in vitro models. Kelm et al. showed how human umbilical cord vein endothelial cells cocultured with human artery-derived fibroblasts can self-assemble into a microtissue vessel with  $\alpha$ -SMA positive fibroblasts lining the lumen due to shear stress.<sup>[60]</sup> Cerchiarai et al. cocultured myoepithelial (MEP) and luminal (LEP) cells with lumenized architecture due to MEP–ECM cohesion that could be altered by tuning LEP–ECM interactions.<sup>[61]</sup> Analogous to natural self-organization processes, where multivariate signals will coordinate complex assembly of multiple cell types, our microconfinement approach identifies conditions that promote the reproducible segregation of cells in vitro, which should prove applicable to other heterotypic cocultures of interest.

## 4. Conclusion

The reproducibility afforded through microengineering techniques provides robust control over stiffness, matrix protein presentation, and geometric cues with consistent surface area that enable self-organization of PDAC and CAF cells. These results highlight the importance of topology at the interface of a growing tumor and how this imbalance of stress could promote CAF activation and migration, as a first in vitro model demonstrating stroma encircling cancer reminiscent of patient histology. Our results identify a relationship between matrix parameters and the cellular organization in coculture that may underlie aspects of pathogenic desmoplasia. This approach will aid fundamental studies of “cell assembly-matrix structure” relationships and provide a tool to develop therapeutic regimens that target PDAC–stroma organization.

## 5. Experimental Section

**Micropatterning Polyacrylamide—Preparing Polyacrylamide Gels:** 2D polyacrylamide (PA) hydrogels were prepared as previously reported.<sup>[15]</sup> Briefly, glass coverslips (18 mm) were functionalized with (3-aminopropyl)triethoxysilane (APTS, Sigma-Aldrich, USA) for 3 min followed by glutaraldehyde (Sigma-Aldrich, USA) for 30 min. PA gels of desired stiffnesses (1, 10, and 100 kPa) were fabricated by combining acrylamide and bis-acrylamide (Sigma, USA) and initiated with 0.1% ammonium persulfate (APS, Sigma, USA) and 0.1% tetramethylethylenediamine (TEMED, Sigma, USA). A 20  $\mu$ L of pregelled solution was dropped onto a hydrophobically treated glass slide and an activated coverslip gently placed on top. After polymerization, the gel-topped coverslip was lifted off the slide taking care not to shear the gel. The surface of the gel was modified with 64% hydrazine hydrate for an hour followed by a 4% acetic acid (1 h) and distilled water wash.

**Contact Printing Micropatterning:** Protein-coated stamps were used to transfer patterns to PA gels. Patterned (circle, flower, star) and nonpatterned PDMS (Polysciences, USA) stamps were fabricated by photolithography. PDMS was cured on a photoresist master pattern (SU-8, MicroChem, USA) created with a laser printed mask and UV exposure. Fibronectin, Collagen I and Laminin (25  $\mu$ g mL<sup>-1</sup>, ThermoFisher Scientific, USA) and sodium periodate (3.5 mg mL<sup>-1</sup>, Univar) were combined in PBS for 45 min to form free aldehydes. This oxidized protein solution was transferred to respective PDMS stamps for a 30 min exposure, then dried with a nitrogen stream. The stamp with remaining protein was briefly humidified and lightly pressed onto the PA gel facilitating the protein immobilization to the hydrazide-modified gel surface. The protein patterned gels were UV sterilized for a minimum of 15 min before cells were seeded.

**Cell Source and Culture—Isolation and Culture of KPC Transgenic Mouse PDAC and CAF Cells from PDAC Tumors:** KPC CAFs were isolated as previously described.<sup>[2,37,62,63]</sup> All animal studies were performed in compliance with Garvan/St. Vincent's Animal Ethics Committee (ARA 19/10) and the Australian code of practice for care and use of animals for scientific purposes. CAFs were validated by immunocytochemistry for GFAP and  $\alpha$ -SMA positivity, and were negative for cytokeratin. KPC CAFs were cultured as per human PDAC CAF culture medium and conditions.<sup>[2,37,63]</sup> Pancreatic cancer cells were cultured with high glucose (4.5 g L<sup>-1</sup> D-glucose) DMEM (Gibco, USA) containing 110 mg L<sup>-1</sup> Na pyruvate and supplemented with 10% foetal bovine serum (FBS) and  $2 \times 10^{-3}$  M GlutaMAX and lifted with 0.25% trypsin. CAFs were cultured with Iscove's modified Dulbecco's medium (IMDM, ThermoFisher Scientific, USA) without phenol red, 10% FBS, and  $4 \times 10^{-3}$  M GlutaMAX and lifted with 0.05% trypsin. Media was changed every two days and cells were passaged at 80–90% confluency, 2–3 times per week.

**Cell Labeling:** Pancreatic cancer cells and CAFs were labeled with CellTracker Green Fluorescent Probe (Lonza, USA) and Red CMPTX (Invitrogen, USA), respectively. After trypsinizing and counting the cells,  $10 \times 10^{-3}$  M CellTracker in dimethyl sulfoxide (DMSO) was added to  $10 \times 10^{-6}$  M final concentration of suspended cells in media, mixing the cells every 5 min for total 30 min exposure. The cells were spun down (300 g, 3 min) and resuspended in warmed media.

**Coculture:** Both pancreatic cancer cells and CAFs were resuspended in warmed cancer cell medium (high-glucose DMEM, 10% FBS, 1% penicillin/streptomycin,  $2 \times 10^{-3}$  M GlutaMAX Gibco, USA). The two cell types were mixed vigorously prior to addition (1 mL) to sterilized, patterned hydrogels in each well of a 12-well polystyrene tissue culture plate. Between each well the cocultured cell suspension was pipetted up and down and the plate swirled to equally distribute the cells over the gels. Cells were culture for 48 h on patterns prior to fixation.

**Small Molecule Inhibitors:** (-)-Blebbistatin (MilliporeSigma) was reconstituted in 90% DMSO at 75 mg mL<sup>-1</sup> stock and diluted to a final 20  $\mu$ M concentration in media. Rock inhibitor Y27632 (ATCC) was prepared with DPBS for a  $10 \times 10^{-3}$  M stock solution and diluted to a 10  $\mu$ M concentration in media. Inhibitor stocks were thawed before adding to a tube of suspended cells, thoroughly mixed, then quickly transferred to the gels for the duration of culture (48 h).

**Imaging—Widefield Live Cell:** Three hours postseeding on micropatterned gels, the 12-well plate of cells on gels was transferred to the widefield box microscope Celldiscoverer7 (Carl Zeiss, Germany) at 37 °C and 5% CO<sub>2</sub> and imaged with an effective 2.5 $\times$  magnification (5 $\times$  objective, 0.5 $\times$  focal magnification changer, 0.35 N.A., air, 5.10 mm working distance) every hour for 48 h.

**Immunofluorescence:** Cells were fixed with 4% paraformaldehyde (Sigma, USA) for 20 min and permeabilized with 0.1% Triton X-100 (Fisher, USA) in PBS for 30 min then blocked with 1% bovine serum albumin (BSA) in PBS for 15 min. Samples were labeled with primary antibodies antiactin,  $\alpha$ -smooth muscle antibody, mouse monoclonal (1:400, Sigma-Aldrich, USA) and anticollagen I, rabbit polyclonal (1:200, ab34710 abcam, USA) in 1% BSA in PBS for 1 h at room temperature, then secondary antibody goat anti-mouse IgG (H+L), Alexa Fluor 647 (1:200, ThermoFisher, USA) and goat anti-rabbit IgG (H+L), Alexa Fluor 555 (1:200, ThermoFisher, USA) in 1% BSA in PBS for 1 h. Gels were mounted on glass slides with DAPI containing fluoroshield mounting media (Sigma, USA) and coated with a layer of clear nail polish to prevent drying prior to imaging. LSM 800 (Carl Zeiss, Germany) inverted Zeiss Axio Observer Z1 laser scanning confocal microscope with 20 $\times$  (0.8 N.A., air, 0.55 mm working distance) objective lens was used to image.

**Atomic Force Microscopy:** The coculture on patterned gel coverslip was washed with 1 $\times$  PBS to remove any debris and/or dead cell and the coverslips were immobilized at the bottom of a 35 mm Fluorodish (World Precision Instruments, USA) and immersed in 1 $\times$  PBS prior to AFM measurements. The JPK Nanowizard 4 XP with Hybrid stage (Bruker, USA) along with the JPK Petridish heater, mounted on a Ti-U inverted optical microscope (Nikon instruments, Japan) within a TMC vibration isolation table (Technical Manufacturing Corporation, MA, USA), with a V-shaped cantilever at a spring constant of 0.35 N m<sup>-1</sup> with a 2  $\mu$ m borosilicate glass particle (Novascan, USA) was used to perform automatized single nanoindentation measurements. Before the experiment, the AFM system was calibrated, the deflection sensitivity of the probe was measured in fluid at 37 °C by engaging the probe on an uncoated glass substrate and the spring constant of the cantilever was determined by a thermal tune sweep. The Young's modulus was extracted from force curves using the Hertz fit with the JPK data processing software (version 7.0.97, Bruker).

**Live Cell Analysis:** Imaris (Oxford Instruments plc, UK) software was used to track widefield live cell images to visualize cell trajectories and generate speed and track straightness data of individual cells on patterns. Time series data were imported and regions of interest masked to track cells within single patterns.

**Heatmap Data Analysis:** ImageJ 1.52p (Fiji is Just, NIH, USA) software was used to analyze immunofluorescence images to generate heatmaps

as previously described.<sup>[15]</sup> Raw images were imported and background subtracted. A minimum of 6 patterns were stacked and translated to align all stacks. Then a z project of the stack was converted to 16 colors lookup table.

**Cell Count:** Quantitative Pathology & Bioimage Analysis (QuPath v0.2.0-m9)<sup>[64]</sup> was used to count nuclei and fluorescent green pancreatic cancer cells. Cells on patterns were analyzed by preprocessing simple tissue detection then watershed cell detection with optimized threshold values was checked by eye for DAPI and Green detection channels. Pancreatic CAF numbers were calculated by subtracting total nuclei from cancer cell.

**Radial Analysis:** ImageJ plugin radial reslice (radial\_reslice\_with\_plot\_v100, DART Microscopy Core at NYU Health, USA) of pancreatic cancer and CAF cell heatmaps (average z project multiple pattern repeats). A central point was selected by coordinates and a gray value versus pixel distance generated.

**Fluorescence Intensity Analysis:** Mean fluorescence intensity values were measured from  $\alpha$ -SMA channel patterns. An inner circle ROI was drawn and area (%) compared to the total pattern held constant across a single shape for analysis. An outer circle ROI was drawn to encompass the entire pattern and integrated density calculated by subtracting the outer from the inner density divided by the area to yield an outer ring mean density. A vertical 223  $\mu$ m line was drawn to determine the mean intensity across the diameter of individual patterns for the respective channels.

**Modeling:** FE models were developed for each micropattern (circle, flower, star) for simulating the mechanoenvironment between the substrate gel and the cancerous, noncancerous cells alone, as well as the coculturing of cancerous and noncancerous cells scenario. The 3D geometries of the FE models were constructed by segmenting the micropatterns in ScanIP N-2018.03 (Simpleware, Exeter, UK) based on SEM images, and then converted into solid assemblies, that contain a patterned contractile layer (cell layer) and a passive layer (gel layer), by using nonuniform rational B-spline (NURBS) patches.

The assemblies were imported into ABAQUS 6.14.1 (Dassault Systèmes, Waltham, USA) and meshed with quadratic tetrahedral elements (C3D10) to smoothly capture the geometric details with an adaptive mesh in a global seed size of 20  $\mu$ m, while particularly intensified mesh refinement (seed size: 1  $\mu$ m) was applied to the cell–micropattern interfaces. The average number of elements was 1471886 (with a degree of freedom of 6302603).

Both the contractile layer and the passive layer were treated as isotropic, linear elastic materials. Based on the in-house AFM experiments, the passive layer (5  $\mu$ m thick) was assigned with a Young's modulus of 10 kPa and a Poisson's ratio of 0.49; the noncancerous contractile layer (20  $\mu$ m) was assigned with values of 0.52 kPa and 0.49 for Young's modulus and Poisson's ratio, respectively, whereas the cancerous contractile layer (20  $\mu$ m) was with values of 0.97 kPa and 0.49. The thermal conductivity and expansion coefficient of the contractile layers were all set as 10 W m<sup>-1</sup> K<sup>-1</sup> and 0.05 K<sup>-1</sup>,<sup>15,47</sup> respectively.

To simulate the mechanoenvironment induced by cellular contraction, the contractile layers were subjected to an isotropic 5 K temperature drop, while the passive layers were fully constrained at the bottom surface.

**Statistics:** GraphPad Prism 8.0.2 was used for plotting and statistical analysis. No outliers were removed. Heatmap sample size was a minimum of six ( $n = 6$ ) for flower with nine ( $n = 9$ ) for circle and star patterns with average  $\pm$  standard deviation. Representative images were selected for stiffness and inhibitor visualization. Data were tested for normality using a Shapiro-Wilk test. An ordinary one-way ANOVA was run with significance determined from a Tukey's multiple comparisons test.

## Supporting Information

Supporting Information is available from the Wiley Online Library or from the author.



## Acknowledgements

The authors thank the Pancreatic Cancer Translational Research Group (PCTRG) for insightful discussions. The authors acknowledge the facilities and scientific and technical assistance of the Biomedical Imaging Facility (BMIF) of the Mark Wainwright Analytical Center at UNSW. This work was supported by funding from the National Health and Medical Research Council (NHMRC) Ideas Grant (Kilian, APP1185021), the National Cancer Institute of the National Institutes of Health (Kilian, R01CA251443), NHMRC project grant (Phillips, APP1144108), Cancer-Institute NSW CDF (Sharbeen, CDF181166), Cancer Australia (Phillips, APP1126736), Translational Cancer Research Network and UNSW Sydney Scientia Ph.D. Scholarship (Nemec). S.N., Q.L., and K.A.K. designed the experiments. P.T., J.Y., G.S., and P.A.P. provided cell material and data analysis. S.N., J.L., J.Z., and C.H. performed the experiments and analyzed the data. All authors contributed to writing the manuscript.

## Conflict of Interest

The authors declare no conflict of interest.

## Data Availability Statement

The data that support the findings of this study are available from the corresponding author upon reasonable request.

## Keywords

cancer-associated fibroblasts, heterotypic cocultures, micropatterning, pancreatic ductal adenocarcinoma

Received: November 12, 2020

Revised: February 18, 2021

Published online:

- [1] P. Phillips, *Transworld Res. Network* **2012**, *37*, 29.
- [2] A. Vonlaufen, S. Joshi, C. Qu, P. A. Phillips, Z. Xu, N. R. Parker, C. S. Toi, R. C. Pirola, J. S. Wilson, D. Goldstein, M. V. Apte, *Cancer Res.* **2008**, *68*, 2085.
- [3] J. A. McCarroll, S. Naim, G. Sharbeen, N. Russia, J. Lee, M. Kavallaris, D. Goldstein, P. A. Phillips, *Front. Physiol.* **2014**, *5*, 141.
- [4] B. Z. Stanger, M. Hebrok, *Gastroenterology* **2013**, *144*, 1170.
- [5] M. B. Omary, A. Lugea, A. W. Lowe, S. J. Pandol, *J. Clin. Invest.* **2007**, *117*, 50.
- [6] E. Sahai, I. Astsaturov, E. Cukierman, D. G. Denardo, M. Egeblad, R. M. Evans, D. Fearon, F. R. Greten, S. R. Hingorani, T. Hunter, R. O. Hynes, R. K. Jain, T. Janowitz, C. Jorgensen, A. C. Kimmelman, M. G. Kolonin, R. G. Maki, R. S. Powers, E. Puré, D. C. Ramirez, R. Scherz-Shouval, M. H. Sherman, S. Stewart, T. D. Tlsty, D. A. Tuveson, F. M. Watt, V. Weaver, A. T. Weeraratna, Z. Werb, *Nat. Rev. Cancer* **2020**, *20*, 174.
- [7] A. Masamune, T. Shimosegawa, *Clin. Res. Hepatol. Gastroenterol.* **2015**, *39*, S98.
- [8] C. Shi, F. C. Pan, J. N. Kim, M. K. Washington, C. Padmanabhan, C. T. Meyer, J. L. Kopp, M. Sander, M. Gannon, R. D. Beauchamp, C. V. Wright, A. L. Means, *CMGH* **2019**, *8*, 579.
- [9] A. D. Rhim, E. T. Mirek, N. M. Aiello, A. Maitra, J. M. Bailey, F. Mcallister, M. Reichert, G. L. Beatty, A. K. Rustgi, R. H. Vonderheide, S. D. Leach, B. Z. Stanger, *Cell* **2012**, *148*, 349.

- [10] J. M. Northcott, I. S. Dean, J. K. Mouw, V. M. Weaver, *Front. Cell Dev. Biol.* **2018**, *6*, 17.
- [11] L. Wullkopf, A.-K. V. West, N. Leijnse, T. R. Cox, C. D. Madsen, L. B. Oddershede, J. T. Erler, *Mol. Biol. Cell* **2018**, *29*, 2378.
- [12] Y. Tan, A. Tajik, J. Chen, Q. Jia, F. Chowdhury, L. Wang, J. Chen, S. Zhang, Y. Hong, H. Yi, D. C. Wu, Y. Zhang, F. Wei, Y.-C. Poh, J. Seong, R. Singh, L.i.-J. Lin, S. Doğanay, Y. Li, H. Jia, T. Ha, Y. Wang, B. O. Huang, N. Wang, *Nat. Commun.* **2014**, *5*, 4619.
- [13] J. M. Northcott, I. S. Dean, J. K. Mouw, V. M. Weaver, *Front. Cell Dev. Biol.* **2018**, *6*, 17.
- [14] D.-H.o Kim, P. P. Provenzano, C. L. Smith, A. Levchenko, *J. Cell Biol.* **2012**, *197*, 351.
- [15] J. Lee, A. A. Abdeen, K. L. Wycislo, T. M. Fan, K. A. Kilian, *Nat. Mater.* **2016**, *15*, 856.
- [16] A. Chronopoulos, T. J. Lieberthal, A. E. Del Río Hernández, *Convergent Sci. Phys. Oncol.* **2017**, *3*, 013001.
- [17] Y. Fan, M. Lesina, H. Algül, *Ann. Transl. Med.* **2020**, *8*, 671.
- [18] J. Li, M. G. Wientjes, J. L.-S. Au, *AAPS J.* **2010**, *12*, 223.
- [19] H. Meng, A. E. Nel, *Adv. Drug Delivery. Rev.* **2018**, *130*, 50.
- [20] J.-H. Lee, S.-K. Kim, I. A. Khawar, S.-Y. Jeong, S. Chung, H.-J. Kuh, *J. Exp. Clin. Cancer Res.* **2018**, *37*, 4.
- [21] M. J. Ware, V. Keshishian, J. L. Law, J. C. Ho, C. A. Favela, P. Rees, B. Smith, S. Mohammad, R. F. Hwang, K. Rajapakshe, C. Coarfa, S. Huang, D. P. Edwards, S. J. Corr, B. Goding, S. A. Curley *Biomaterials* **2016**, *108*, 129.
- [22] C. R. Drifka, K. W. Eliceiri, S. M. Weber, W. J. Kao, *Lab Chip* **2013**, *13*, 3965.
- [23] S.-K. Kim, S. D. Jang, H. Kim, S. Chung, J. K. Park, H.-J. Kuh, *Cancers* **2020**, *12*, 1305.
- [24] T. J. Puls, X. Tan, M. Husain, C. F. Whittington, M. L. Fishel, S. L. Voytik-Harbin, *Sci. Rep.* **2018**, *8*, 13039.
- [25] H. Saini, K. Rahmani Eliato, C. Silva, M. Allam, G. Mouneimne, R. Ros, M. Nikkhah, *Cell. Mol. Bioeng.* **2018**, *11*, 419.
- [26] A. J. Rice, E. Cortes, D. Lachowski, B. C. H. Cheung, S. A. Karim, J. P. Morton, A. Del Río Hernández, *Oncogenesis* **2017**, *6*, e352.
- [27] M. Weniger, K. Honselmann, A. Liss, *Cancers* **2018**, *10*, 316.
- [28] J. Xia, Y. Qiu, X. Xun, L. Ma, J. Guan, M. Su, *Anal. Chim. Acta* **2018**, *1007*, 26.
- [29] M. Versaavel, T. Grevesse, S. Gabriele, *Nat. Commun.* **2012**, *3*, 671.
- [30] J. Fukuda, A. Khademhosseini, J. Yeh, G. Eng, J. Cheng, O. C. Farokhzad, R. Langer, *Biomaterials* **2005**, *27*, 1479.
- [31] S. Mukundan, K. Sharma, K. Honselmann, A. Singleton, A. liss, B. Parekkadan, *Technology in Cancer Research & Treatment* **2018**, <https://doi.org/10.1177/1533033818803632>.
- [32] T. R. Cox, *Nat. Rev. Cancer* **2021**.
- [33] C. Vennin, K. J. Murphy, J. P. Morton, T. R. Cox, M. Pajic, P. Timpson, *Gastroenterology* **2018**, *154*, 820.
- [34] S. Tsai, L. McOlash, K. Palen, B. Johnson, C. Duris, Q. Yang, M. B. Dwinell, B. Hunt, D. B. Evans, J. Gershan, M. A. James, *BMC Cancer* **2018**, *18*, 335.
- [35] J. Lee, A. A. Abdeen, J. Hedhli, K. L. Wycislo, I. T. Dobrucka, T. M. Fan, L. W. Dobrucki, K. A. Kilian, *Sci. Adv.* **2017**, <https://doi.org/10.1126/sciadv.1701350>.
- [36] A. A. Abdeen, J. B. Weiss, J. Lee, K. A. Kilian, *Tissue Eng., Part A* **2014**, *20*, 2737.
- [37] G. Sharbeen, J. A. McCarroll, A. Akerman, C. Kopecky, J. Youkhana, J. Holst, C. Boyer, M. Erkan, D. Goldstein, P. Timpson, T. R. Cox, B. A. Pereira, J. L. Chitty, S. Fey, A. K. Najumudeen, A. D. Campbell, O. J. Sansom, R. M. C. Ignacio, S. Naim, J. Liu, N. Russia, J. Lee, A. Chou, A. Johns, A. Gill, E. Gonzales-Aloy, J. Kokkinos, V. GebSKI, N. Turner, M. Apte, et al., *BioRxiv* **2020**.
- [38] D. Öhlund, A. Handly-Santana, G. Biffi, E. Elyada, A. S. Almeida, M. Ponz-Sarvise, V. Corbo, T. E. Oni, S. A. Hearn, E. J. Lee, I. I. C. Chio, C.-I. Hwang, H. Tiriác, L. A. Baker, D. D. Engle, C. Feig,

- A. Kultti, M. Egeblad, D. T. Fearon, J. M. Crawford, H. Clevers, Y. Park, D. A. Tuveson, *J. Exp. Med.* **2017**, 214, 579.
- [39] H. Y. Tanaka, T. Kurihara, T. Nakazawa, M. Matsusaki, A. Masamune, M. R. Kano, *Biomaterials* **2020**, 251, 120077.
- [40] A. Rubiano, D. Delitto, S. Han, M. Gerber, C. Galitz, J. Trevino, R. M. Thomas, S. J. Hughes, C. S. Simmons, *Acta Biomater.* **2018**, 67, 331.
- [41] M. V. Apte, R. C. Pirola, J. S. Wilson, *Front. Physiol.* **2012**, 3, 344.
- [42] D. Lachowski, E. Cortes, D. Pink, A. Chronopoulos, S. A. Karim, J. P. Morton, A. E. Del Río Hernández, *Sci. Rep.* **2017**, 7, 2506.
- [43] A. Pathak, S. Kumar, *Proc. Natl. Acad. Sci. USA* **2012**, 109, 10334.
- [44] Y. Li, M. J. Fanous, K. A. Kilian, G. Popescu, *Sci. Rep.* **2019**, 9, 248.
- [45] T.-H. Chen, X. Zhu, L. Pan, X. Zeng, A. Garfinkel, Y. Tintut, L. L. Demer, X. Zhao, C.-M. Ho, *Biomaterials* **2012**, 33, 9019.
- [46] J. Fu, Y.-K. Wang, M. T. Yang, R. A. Desai, X. Yu, Z. Liu, C. S. Chen, *Nat. Methods* **2010**, 7, 733.
- [47] C. M. Nelson, R. P. Jean, J. L. Tan, W. F. Liu, N. J. Sniadecki, A. A. Spector, C. S. Chen, *Proc. Natl. Acad. Sci. USA* **2005**, 102, 11594.
- [48] L. Tian, Z.-P. Lu, B.-B. Cai, L.-T. Zhao, D. Qian, Q.-C. Xu, P.-F. Wu, Y. Zhu, J.-J. Zhang, Q. Du, Y. Miao, K.-R. Jiang, *Int. J. Oncol.* **2016**, 48, 783.
- [49] A. Masamune, K. Kikuta, M. Satoh, K. Satoh, T. Shimosegawa, *Br. J. Pharmacol.* **2003**, 140, 1292.
- [50] K. P. Olive, *Clin. Cancer Res.* **2015**, 21, 3366.
- [51] S. Pandol, M. Edderkaoui, I. Gukovsky, A. Lugea, A. Gukovskaya, *Clin. Gastroenterol. Hepatol.* **2009**, 7, S44.
- [52] L. Bolm, S. Cigolla, U. A. Wittel, U. T. Hopt, T. Keck, D. Rades, P. Bronsert, U. F. Wellner, *Transl. Oncol.* **2017**, 10, 578.
- [53] D. Thomas, P. Radhakrishnan, *Mol. Cancer* **2019**, 18, 14.
- [54] K. Kikuta, A. Masamune, T. Watanabe, H. Ariga, H. Itoh, S. Hamada, K. Satoh, S. Egawa, M. Unno, T. Shimosegawa, *Biochem. Biophys. Res. Commun.* **2010**, 403, 380.
- [55] N. Sperb, M. Tsesmelis, T. Wirth, *Int. J. Mol. Sci.* **2020**, 21, 5486.
- [56] H. M. Begum, H. P. Ta, H. Zhou, Y. Ando, D. Kang, K. Nemes, C. F. Mariano, J. Hao, M. Yu, K. Shen, *Sci. Rep.* **2019**, 9, 11187.
- [57] K. Shen, S. Luk, D. F. Hicks, J. S. Elman, S. Bohr, Y. Iwamoto, R. Murray, K. Pena, F. Wang, E. Seker, R. Weissleder, M. L. Yarmush, M. Toner, D. Sgroi, B. Parekkadan, *Nat. Commun.* **2014**, 5, 5662.
- [58] J. Wang, R. Zohar, C. A. Mcculloch, *Exp. Cell Res.* **2006**, 312, 205.
- [59] N. R. London, K. J. Whitehead, D. Y. Li, *Angiogenesis* **2009**, 12, 149.
- [60] J. M. Kelm, V. Lorber, J. G. Snedeker, D. Schmidt, A. Broggini-Tenzer, M. Weisstanner, B. Odermatt, A. Mol, G. Zünd, S. P. Hoerstrup, *J. Biotechnol.* **2010**, 148, 46.
- [61] A. E. Cerchiari, J. C. Garbe, N. Y. Jee, M. E. Todhunter, K. E. Broaders, D. M. Peehl, T. A. Desai, M. A. Labarge, M. Thomson, Z. J. Gartner, *Proc. Natl. Acad. Sci. USA* **2015**, 112, 2287.
- [62] J. P. Morton, P. Timpson, S. A. Karim, R. A. Ridgway, D. Athineos, B. Doyle, N. B. Jamieson, K. A. Oien, A. M. Lowy, V. G. Brunton, M. C. Frame, T. R. J. Evans, O. J. Sansom, *Proc. Natl. Acad. Sci. USA* **2010**, 107, 246.
- [63] M. G. Bachem, E. Schneider, H. Groß, H. Weidenbach, R. M. Schmid, A. Menke, M. Siech, H. Beger, A. Grünert, G. Adler, *Gastroenterology* **1998**, 115, 421.
- [64] P. Bankhead, M. B. Loughrey, J. A. Fernández, Y. Dombrowski, D. G. Mcart, P. D. Dunne, S. Mcquaid, R. T. Gray, L. J. Murray, H. G. Coleman, J. A. James, M. Salto-Tellez, P. W. Hamilton, *Sci. Rep.* **2017**, 7, 16878.